Astronomy & Astrophysics manuscript no. amirocha
July 4, 2019
©ESO 2019

Signatures of UV radiation around low-mass protostars in the Serpens Main with IRAM 30m

Agnieszka Mirocha[1,2], Agata Karska[2], Lars E. Kristensen[3], Marcin Gronowski[4], Miguel Figueira[5], Marcin Gładkowski[2,6], and Michał Żółtowski[2]

[1] Astronomical Observatory of the Jagiellonian University, ul. Orla 171, 30-244 Kraków, Poland
e-mail: amirocha@doctoral.uj.edu.pl
[2] Centre for Astronomy, Faculty of Physics, Astronomy and Informatics, Nicolaus Copernicus University, ul. Grudziądzka 5, 87-100 Toruń, Poland
[3] Centre for Star and Planet Formation, Niels Bohr Institute and Natural History Museum of Denmark, University of Copenhagen, Øster Voldgade 5-7, DK-1350 Copenhagen K, Denmark
[4] Faculty of Physics, University of Warsaw, ul. Pasteura 5, 02-093 Warszawa, Poland
[5] National Centre for Nuclear Research, ul. Pasteura 7, 02-093 Warszawa, Poland
[6] Nicolaus Copernicus Astronomical Center, ul. Rabiańska 8, 87-100 Toruń, Poland

Received [Month] [Day], 2019; accepted [Month] [Day], 2019

ABSTRACT

Context. The Serpens Main is one of the most studied star forming region containing low-mass protostars. Observations at submillimetre range allow to determine physical and chemical processes around young stellar objects.
Aims. We aim to characterise the UV radiation in the surroundings of the low-mass protostars. We analyse the exitation and spatial extend of HCN, CN, CS and their isotopologues to identify the underlying processes. We can investigate the feedback from protostars and the excitation mechanism of molecules.
Methods. We present 30 arcmin^2 IRAM 30m maps of CN $J = 1 - 0$, HCN $J = 1 - 0$, and CS $J = 3 - 2$ encompassing 10 low-mass protostars. We calculated HCN $J = 1 - 0$ and CN $J = 1 - 0$ column densities around low-mass protostars and selected outflows positions using the RADEX radiative transfer code. The obtained column densities were compared with the astrochemical model of molecules abundaces in order to characterise UV radiation field.
Results. Emission of HCN $J = 1 - 0$ and CS $J = 3 - 2$ is co-spatial with outflows, CN emission peaks at the positions of protostars. CN $J = 1 - 0$ and HCN $J = 1 - 0$ column densities were estimated as 10^{13}-10^{14}cm^{-2}. Regardless of gas parameters CN/HCN column density ratio was modeled in range of 1-10. This result can be reproduced by providing an additional UV radiation source of 0.044 to 0.001 G_0.
Conclusions. As a product of HCN photodissociation CN molecules indicate bow shocks around young stellar objects. The astrochemical model obtained with the Nahoon code shows that an additional source of UV radiation is needed to cover the abundances range indicated by observations.

Key words. astrochemistry – stars: formation – ISM: molecules – ISM: individual objects: Sepens Main – Submillimeter: ISM

1. Introduction

2. Observations

The Serpens Main star forming region was observed with IRAM 30 between 14 and 17 July 2009 (project no. xxx, PI: L. Kristensen). We used the Eight MIxer Receiver (EMIR) as the frontend. The observations were performed in the EMIR bands E090 (molecule HCN $J = 1 - 0$) covering the range 73-117 GHz and E150 (molecules CN $J = 1 - 0$ and CS $J = 3 - 2$) covering the frequencies between 125 and 184 GHz. Due to the EMIR receiver wide bands additional molecular lines of $C^{34}S$ $J = 3 - 2$, $H^{13}CN$ $J = 1 - 0$ and $H^{13}CN$ $J = 2 - 1$ were also observed. The backend was the Versatile SPectrometer Array (VESPA) autocorrelator and the 1 MHz filterbank reaching the spectral resolution of 39 kHz (E150 band) and 78 kHz (E090 band). The telescope beam size varies from 14″ at 172.68 GHz to 29″ at 86.34 GHz (Table 1). The antenna temperatures were converted to main-beam brightness temperature T_{MB} using the main beam efficiency according to the expresion: $T_{MB} = T_A/\eta_{MB}$. The exact upper levels enegies, line frequencies, beam sizes and beam efficiencies are given in Table 1. Observations included scans of the Ser-SMM1 (centered at $\alpha_{J2000} = 18^h29^m49.6^s$, $\delta_{J2000} = +01°15'20.5''$ with $V_{LSR} = +8.5$ km/s) and the Ser-SMM3/Ser-SMM4 (centered at $\alpha_{J2000} = 18^h29^m56.6^s$, $\delta_{J2000} = +01°14'00.3''$ with $V_{LSR} = +7.6$ km/s) regions, both 1′×3′ OTF maps. The size of the maps is about 300″ × 350″, covering both Ser-SMM1 and Ser-SMM3/Ser-SMM4 regions. The regions are referenced in the article as 'the Northen part' and 'the Southern part' respectively.

Data reduction was carried out with the CLASS package within GILDAS[1]. Each spectrum was corrected for the baseline shape, the spike channels were removed and the velocity was resampled to a resolution of 0.5 km/s. The baseline fitting of the order of 0 was sufficient for our observations. The rms of extracted spectra values vary from 0.024 K to 0.125 K. Both OTF

[1] See http://www.iram.fr/IRAMFR/GILDAS

Table 1. Overview of the observations

Mol.	Trans.	E_u (K)	Freq. (GHz)	Beam size ($''$)	Beam eff. η_{MB}
HCN	1-0	4.25	88.631602	28	0.81
CN	1-0	5.45	113.494921	22	0.78
CS	3-2	14.1	146.969029	16	0.74
$C^{34}S$	3-2	13.9	144.617109	16	0.74
$H^{13}CN$	1-0	4.14	86.342274	29	0.81
$H^{13}CN$	2-1	12.43	172.677881	14	0.68

Notes. Beam sizes and efficiencies are taken from http://www.iram.es/IRAMES/mainWiki/Iram30mEfficiencies

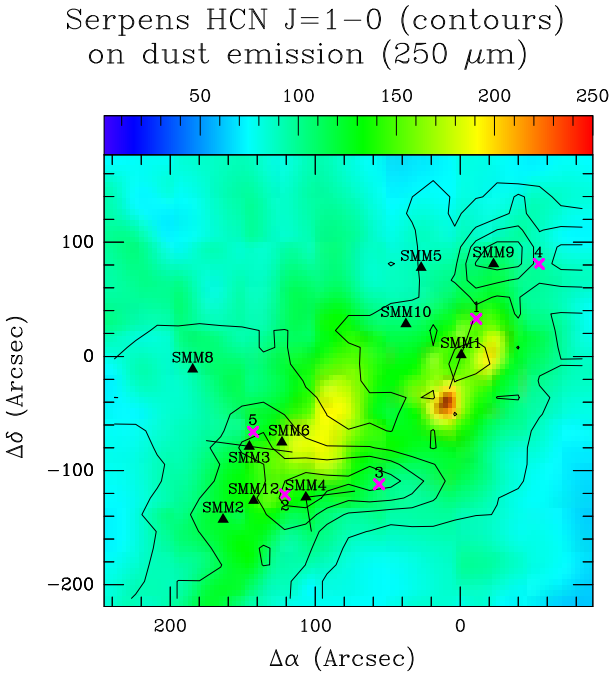

Fig. 1. Dust emission + HCN.

maps were merged in one map covering 300×350 arcsec. The spectra obtained were exported from the CLASS package and analysed with Python scripts.

3. Results

3.1. Physical properties of embedded protostars

Ten Class 0/I protostars are present in the observed region. There are deeply embedded sources so the radiation coming from theirs neighbourhood is highly absorbed in the envelopes, than re-emited in the IR range. Envelopes become thinner with time, thus Spectral Energy Distributions (SEDs) allow to estimate the evolutional stage of an object (André et al. 2000).

A broad-band observations are needed in order to determine physical properties od protostar. Based on SEDs the bolometric temperature and luminosity can be calculated for each of observed protostars. Most of the protostars in our sample have not been investigated for their physical properties. Only SMM1, SMM3 and SMM4 were covered by PACS spectroscopy (Karska et al. 2013) as part of the 'Water in star-forming regions with Herschel' (WISH[2]) key program (van Dishoeck et al. 2011).

The SED plots (Fig. 2) were prepared based on literature samples (Dunham et al. 2015, Karska et al. 2013) and the data from the Herschel Gould Belt survey project (André et al. 2010). Some of the protostars in our sample can be associated with Ser-emb sources observed with the c2d and Bolocam project (Enoch et al. 2007, Enoch et al. 2009). The additional Herschel data cover the SED peak, therefore provide a more detailed information allowing to calculate the bolometric temperatures and luminosities of the protostar more precisely.

The linear interpolation was performed while calculating the protostars parameters. The bolometric luminosity was determined by integrating the SEDs over frequency:

$$L_{bol} = \pi\, d^2 \int F_\nu d\nu \tag{1}$$

where d is the cloud distance of 436 ± 9.2 pc (Ortiz-León et al. 2017). The bolometric temperature was calculating as described in Myers and Ladd 1993:

$$T_{bol} = 1.25\, 10^{-11}\, \bar{\nu} \tag{2}$$

where $\bar{\nu}$ is the mean frequency given by:

$$\bar{\nu} = \frac{\int \nu F_\nu d\nu}{\int F_\nu d\nu} \tag{3}$$

Table 2 contains the observed protostars parameters as well as the Class classification. The classification was adopted from Enoch et al. 2009 where four types of protostars with envelopes were distinguished. Early Class 0 was defined as a protostar of bolometric temperature lesser than 50 K. Prostostars characterised by bolometric temperature between 50 K and 100 K were classified as Late Class 0 protostars. Class I protostars were divided for Early and Late sub-type by the bolometric temperature of 300 K.

Most of the observed protostars in the Serpens Main region are very young, embedded sources of Early Class 0. SMM5 and SMM12 were classified as Early Class I YSOs. The SMM6 protostar is the most evolved object in our sample.

3.2. Molecular emission maps

The line maps in the targeted molecules show variety of structures that can be associated with YSOs and a large-scale cloud emission. Different spatial extend in molecules radiation is connected with various physical conditions around protostars. Here, we present the large-scale maps of CS $J = 3-2$, HCN $J = 1-0$ and CN $J = 1-0$. Maps of their isotopologues are shown in the Appendix A.

Outflows associated with low-mass protostars (Table 2) are observed in certain molecules emission. Blue- and redshifted molecular outflows around Ser-SMM1, Ser-SMM3 and Ser-SMM4 were pointed based on CO $J = 6-5$ and CO $J = 3-2$ observations (Yıldız et al. 2015). Additionally, five outflows positions were selected to more detailed studies (Table 3).

The integrated line intensity map of HCN $J = 1-0$ (Fig. 3) shows extended emission along outflow directions. The HCN $J = 1-0$ line was detected at all positions, although it is weak at

[2] WISH observes about 80 protostars at different evolutionary stages and masses with HIFI and PACS instruments on-board the Herschel Space Observatory.

Table 2. Catalogue of protostars properties

R.A. (J2000.0)	Decl. (J2000.0)	Source	T_{bol} (K)	L_{bol} ($L_\odot$)	Class	Other names
18 29 48.3	+01 16 42.7	SMM9	46.1	11.7	Early Class 0	ISO241, WMW23
18 29 50.0	+01 15 20.3	SMM1	40.4	108.7	Early Class 0	FIRS1, Ser-emb6, Bolo23, EC41
18 29 51.4	+01 16 38.3	SMM5	148.2	4.5	Early Class I	EC53, WMW24, Ser p3
18 29 52.3	+01 15 48.8	SMM10	85.0	5.1	Late Class 0	WMW21
18 29 57.0	+01 13 11.3	SMM4	29.5	13.6	Early Class 0	
18 29 57.8	+01 14 05.3	SMM6	526.4	43.4	Late Class I	EC90, WMW35, SVS20S
18 29 59.1	+01 13 14.3	SMM12	100.9	6.7	Early Class I	
18 29 59.6	+01 13 59.2	SMM3	42.4	27.5	Early Class 0	
18 30 00.5	+01 12 57.8	SMM2	41.6	5.1	Early Class 0	Ser-emb4, Bolo28
18 30 01.9	+01 15 09.2	SMM8		0.068[a]		

Coordinates taken from Suresh et al. 2016, except S68N (Enoch et al. 2007) and SMM8 (Lee et al. 2014).
References: [a]Dionatos et al. 2010

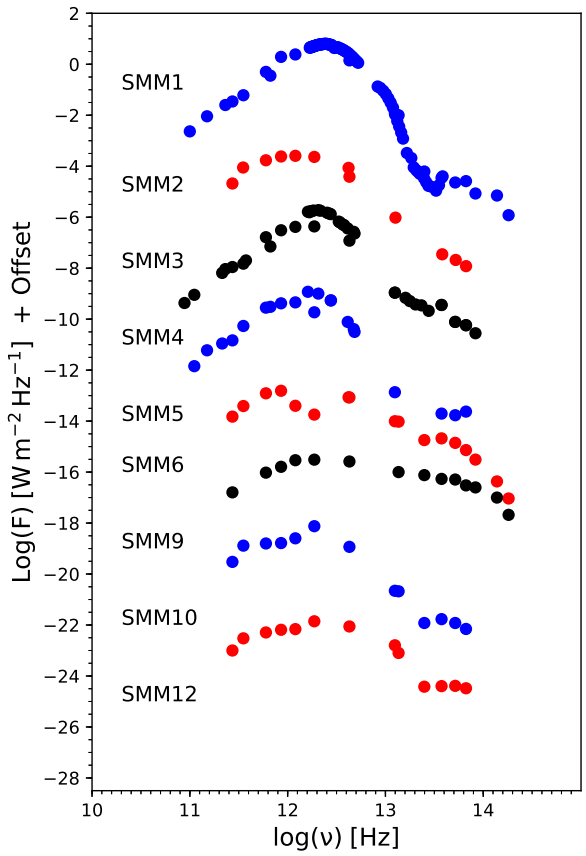

Fig. 2. Spectral Energy Distributions of protostars in the Serpens Main region.

the positions of Ser-SMM5 and Ser-SMM10. On the other hand, the HCN $J = 1 - 0$ emission is particularly strong around Ser-SMM4 and Ser-SMM9 sources. The emission maxima are detected among the known outflows of Ser-SMM1 and Ser-SMM4 (Yıldız et al. 2015). Especially, at the end of Ser-SMM4 blue outflow (position no. 4) we have significantly strong maximum of the HCN $J = 1 - 0$. There is no intensively elongated outflow structure from Ser-SMM3 source.

CS $J = 3 - 2$ line emission map (Fig. 4) shows similar spatial distribution to HCN $J = 1 - 0$. The most significant elongated structure can be associated with Ser-SMM4 blue-shifted outflow.

Table 3. Properties of the selected off-source positions

Pos.	R.A. (J200)	Decl. (J200)	Remarks
1	18:29:45.47	+01:15:53.5	SMM1 blue-shifted outflow in CO $J = 3 - 2$
2	18:29:54.66	+01:13:19.5	max. CN $J = 1 - 0$, SMM4 blue-shifted outflow in CO $J = 3 - 2$
3	18:29:50.33	+01:13:68.5	max. HCN $J = 1 - 0$, SMM4 blue-shifted
4	18:29:43	+01:16:41.5	outflow visible in $C^{34}S$(3-2)
5	18:29:56.13	+01:14:14.5	max. CN $J = 1 - 0$, SMM9 surroundings

It is situated at the same place in both maps, extending over 80″. A similar large-scale structure is detected along Ser-SMM1 outflows, although it is much more distinctive in the HCN $J = 1 - 0$ map. A strong emission around Ser-SMM9 have a circular shape in HCN $J = 1 - 0$ map, however, it has more elongated structure in CS $J = 3 - 2$ line emission which overlaps with the S68N outflows (Kristensen et al. 2010). The peaks of emissions are situated in the different places. HCN $J = 1 - 0$ has relatively strong emission around Ser-SMM4 protostar, but in CS $J = 3 - 2$ line a significant emission towards position no. 3 can be noticed that indicates CN $J = 1 - 0$ local maximum.

CN $J = 1 - 0$ line emission is focused mostly around the positions of protostars (Fig. 5). The highest local peaks are associated with Class 0 low-mass protostars: Ser-SMM1 (8.2 K km/s), Ser-SMM3 (15.9 K km/s), Ser-SMM4 (14.1 K km/s) and Ser-SMM6 (15.3 K km/s). The spatial distribution is qualitatively different compared to the HCN $J = 1 - 0$ map. The strongest emission characterises the dense surroundings of Ser-SMM3, Ser-SMM6 and Ser-SMM4 sources while the northern part of this region does not show such a distinct emission in the HCN $J = 1 - 0$ line. On the other hand, dense emissive region of the Ser-SMM9 source is significantly weaker in CN $J = 1 - 0$ line. CN $J = 1 - 0$ map can be characterised by compact, condensed emission without any strongly elongated structures. The $H^{13}CN$ $J = 1 - 0$ line exhibits similar morphological distribution as CN(1-0) and $C^{34}S$(3-2).

In the presence of the UV radiation, HCN molecule photodissociates into CN molecule and H atom (Stäuber et al. 2005).

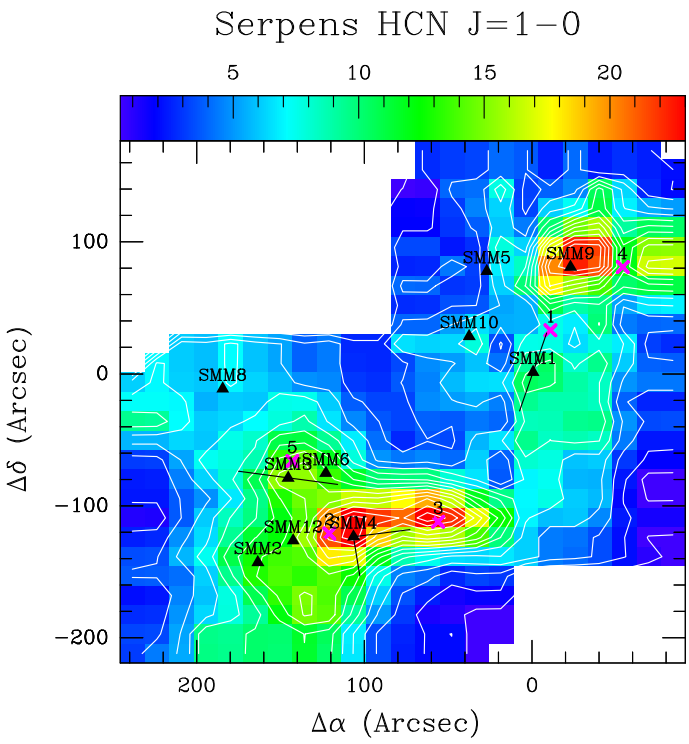

Fig. 3. Emission of the HCN $J = 1 - 0$ in the Serpens Main region. Black triangles show the positions of the protostars (Suresh et al. 2016), whereas the black lines show the associated outflow directions (Yıldız et al. 2015). Outflow positions were displayed as pulrple crosses.

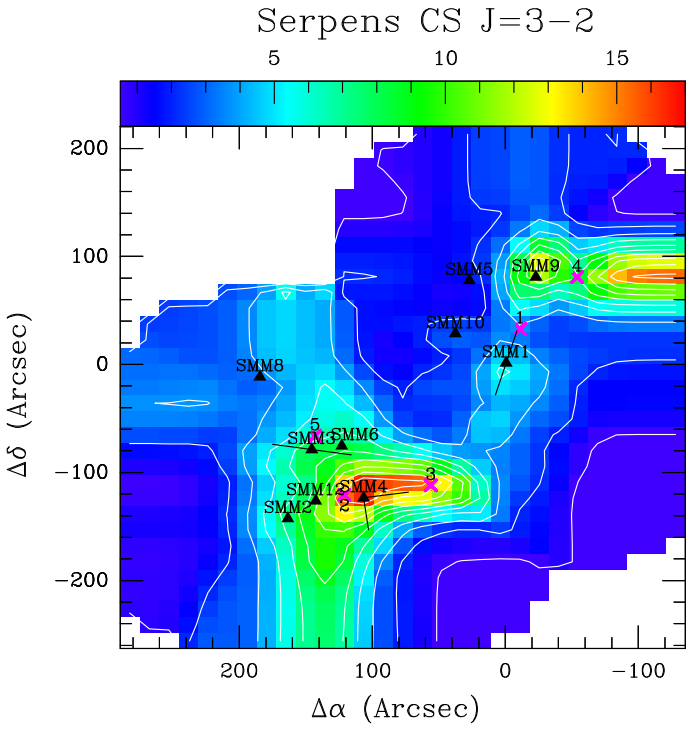

Fig. 4. Similar to Fig. 3 but the emission of the CS $J = 3 - 2$ line.

Thus, combined map of these molecules can indicate regions with stronger UV radiation. We present a large-scale map of CN $J = 1 - 0$ to HCN $J = 1 - 0$ flux ratio (Fig. 6). The image of CN emission has been resampled to beam size of HCN in order to compare the same emitting regions. CN/HCN ratio is relatively low around the brightest submillimetre source Ser-SMM1. Similarly, at the dense area of Ser-SMM9 surrounding a significantly weaker CN/HCN emission can be noticed. On the other hand, it peaks at the Northern part of the map around rather faint Ser-SMM5 source. At the Southern part high CN/HCN ratio emission is more extended than in the Northen part. It expands from Ser-SMM3 and Ser-SMM6 area to the North. High CN/HCN ratio can also be found on the edges of the image but it is probably caused by different size of the CN and the HCN maps.

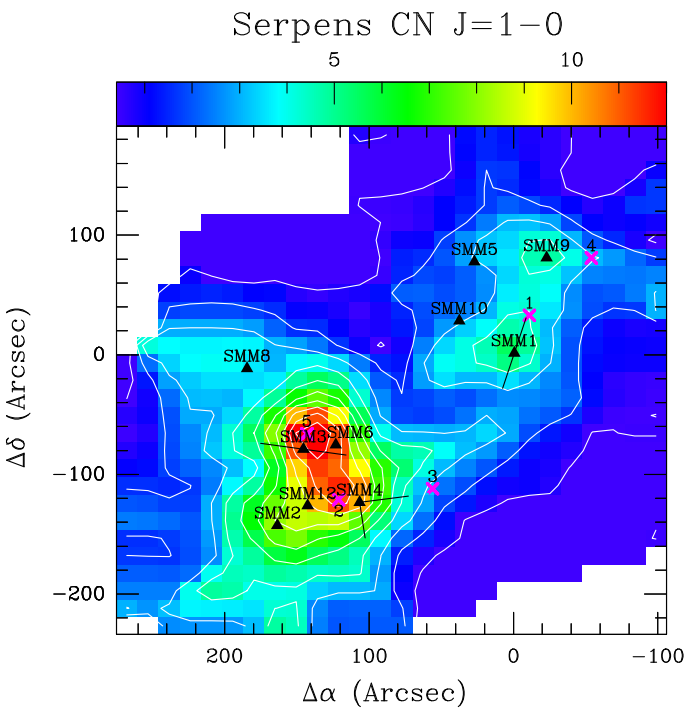

Fig. 5. Similar to Fig. 3 but the emission of the CN $J = 1 - 0$ line.

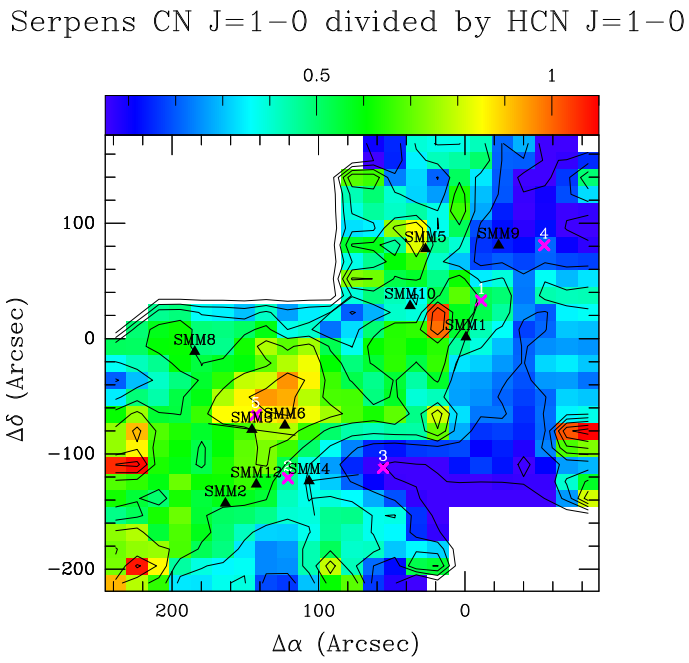

Fig. 6. Emission of the divided fluxes CN $J = 1 - 0$/HCN $J = 1 - 0$ in the Serpens Main region. Black triangles show the positions of the protostars (Suresh et al. 2016), whereas the black lines show the associated outflow directions (Yıldız et al. 2015). Outflow positions were displayed as pulrple crosses.

The low energy level of HCN (E_u = 4.25 K) traces cold, high-density gas. HCN has previously been shown to be a good tracer of molecular outflows activity (Walker-Smith et al. 2014). Similar spatial distribution is presented in the CS map. It means that both species trace the gas of the same properties. The CN line is similarly low-energetic, however it peaks in different areas than HCN and CS. CN as a product of HCN photodissotiation indicates other properties of low-mass protostars surroundings (Section 4).

To summarise, spatial distribution of different lines emission varies depending on the observed molecule. The most distinct differences can be noticed between HCN and CN map. Most of the sources show high flux values in both molecules (Table 4). However, they present unequal levels which indicates regions of different properties. In order to better understand this issue we analyse the molecular line profiles in the Section 3.2.

3.3. Line profiles

We selected 14 representative on-source and off-source positions for a detailed analysis (Fig. 7). Nine of them are corresponding to the protostars positions, the other five off-source positions were selected based on local maximum of the flux.

The mean region is consistent with HCN $J = 1-0$ beam size (27.8") for all molecules. In the majority of our sources five of targeted lines were detected: CN $J = 1-0$, HCN $J = 1-0$, CS $J = 3-2$, $C^{34}S$ $J = 3-2$ and $H^{13}CN$ $J = 1-0$. The line is considered to be detected if there is an emission at the level of at least 3σ. A weak emission from $H^{13}CN$ $J = 2-1$ was found at the positions of four sources and it is not included in the Figure.

The strongest emission occurs in HCN $J = 1-0$, CN $J = 1-0$ and CS $J = 3-2$ lines and it was detected at the position of all of the sources. The emission in the other lines was multiplied in order to compare profiles between different molecules. In HCN, CN species and their isotopologues a few different velocity components can be identified what indicates the hyperfine splitting. This occurs if a molecule has a non-zero nuclear spin so there is also an interaction between the nuclear spin and the electronic angular momentum. The most distinct splitting can be spotted in the CN $J = 1-0$ profiles with five separate components situated between -70 km/s and 18 km/s. The HCN $J = 1-0$ line is characterised by three components with low separation situated in the range of -2 km/s – 16 km/s.

Ser-SMM1, Ser-SMM9, and Ser-SMM10 sources have wide spectral lines, while others exhibit narrow line profiles. Spectra extracted form Positions no. 1, 4 and 5 shows prominent blue-shifted wings what can be associated with outflows. Similar structure can be noticed in the Ser-SMM3 (panel no. 7) CS 3-2 and HCN $J = 1-0$ profiles.

4. Analysis

4.1. Lines column densities

Table 4 shows fluxes integrated from the average line profile at the positions of known protostars. Flux calculation in individual lines allows us to determine the column density of a given transition. The column density of the upper level N_{up} of each observed line was calculated based on following relation:

$$N_u = \beta \frac{\nu W}{A} \quad (4)$$

where $\beta = 1937$ cm^{-2} and $W = \int T_{mb}\, dV$ is the integrated intensity of the emission line. The frequency ν should be given in GHz.

The column densities of the upper level of CN $J = 1-0$ and HCN $J = 1-0$ transitions are presented in Table 4. In the closest surroundings of low-mass protostars CN $J = 1-0$ is stronger than the lowest transition line of HCN. The column density of CN $J = 1-0$ varies between 10^{14} -10^{15} cm^{-2}, while in the column density of the HCN's lowest transition reaches 10^{14} cm^{-2} . Except for the Ser-SMM9 and the Ser-SMM10 neighbourhood, HCN $J = 1-0$ line column density is an order of magnitude lower than the column density of the equivalent CN transition. This result provides a clue to better understand of the low-mass protostars chemistry.

4.2. RADEX modelling

Molecules column densities can be independently determined using molecular excitation models. Line ratio can provide additional information concerning physical properties of the observed gas.

The non-LTE radiative transfer code RADEX (van der Tak et al. 2007) was run in order to prepare sets of molecular excitation models. The CN and HCN molecules column density ratio was the only free parameter. HCN column density was chosen as 10^8 cm^{-2} in order to ensure optically thin emission. CN column density parameter varies from 10^6 cm^{-2} to 10^{10} cm^{-2} what translates into N_{CN}/N_{HCN} in following limits: 10^{-2}-10^2. The sets of models were developed assuming a line width of 1.0 km s^{-1}, hydrogen densities of $n_{H_2} = 10^3$ cm^{-3}, $n_{H_2} = 10^4$ cm^{-3} and $n_{H_2} = 10^5$ cm^{-3} and kinetic temperatures of $T_{kin} = 30$ K, $T_{kin} = 75$ K and $T_{kin} = 200$ K. The molecular data files used during modelling were procured from the Leiden Atomic and Molecular Database (LAMDA, Schöier et al. 2005).

Fig. 8 presents one exemplary set of models of CN/HCN column density ratio versus the modelled line intensities ratio for hydrogen densities of $n_{H_2} = 10^5$ cm^{-3} and kinetic temperatures of $T_{kin} = 200$ K. The rest of the models are shown in the Appendix B. CN/HCN column density ratio weakly depends on hydrogen density and kinetic temperature in the low limit of those parameters. All presented models show similar properties.

The modelled line intensities are compared with the observations. The observed line intensity ratio covers a range of 0.0-1.0 of the column density ratio in the logarithmic scale. That corresponds to a few times higher CN column density than the same parameter of HCN. This result slightly depends on hydrogen densities and kinetic temperature of the gas (see Table 5).

The sets of models shown in this section indicate that CN/HCN column density ratio covers the range of 1-10 regardless of excitation conditions. This result suggests that the UV radiation may play an important role around low-mass protostars.

4.3. Astrochemical model

In Section 4.2 we have raised a question about influence of the UV radiation on the surrounding of the observed sources. A simply astrochemical model can be obtained in order to estimate the intensity of the UV field in reference to units of the interstellar UV field G_0.

HCN easily photodissotiates into CN molecule and H atom. On the other hand, CN needs more energetic photon for disintegration. In the presence of the UV photons HCN can be disso-

Table 4. Integrated fluxes of the observed line at the positions of protostars

Source	Line	Flux (K)	Column dens. (cm^{-2})
SMM1	CN 1-0	6.53	1.3×10^{15}
	HCN 1-0	6.78	1.9×10^{14}
	CS 3-2	6.93	7.9×10^{13}
	$C^{34}S$ 3-2	1.39	1.7×10^{13}
	$H^{13}CN$ 1-0	1.28	no data
	$H^{13}CN$ 2-1	0.03	no data
SMM2	CN 1-0	10.58	2.2×10^{15}
	HCN 1-0	13.98	4.0×10^{14}
	CS 3-2	8.03	9.1×10^{13}
	$C^{34}S$ 3-2	1.15	1.4×10^{13}
	$H^{13}CN$ 1-0	2.46	no data
	$H^{13}CN$ 2-1	not detected	
SMM3	CN 1-0	13.26	2.7×10^{15}
	HCN 1-0	12.48	3.6×10^{14}
	CS 3-2	10.04	1.1×10^{14}
	$C^{34}S$ 3-2	0.37	4.4×10^{12}
	$H^{13}CN$ 1-0	0.98	no data
	$H^{13}CN$ 2-1	not detected	
SMM4	CN 1-0	13.06	2.7×10^{15}
	HCN 1-0	20.20	5.7×10^{14}
	CS 3-2	19.81	2.2×10^{14}
	$C^{34}S$ 3-2	0.02	1.9×10^{11}
	$H^{13}CN$ 1-0	2.10	no data
	$H^{13}CN$ 2-1	0.26	no data
SMM5	CN 1-0	2.57	3.2×10^{14}
	HCN 1-0	3.71	1.1×10^{14}
	CS 3-2	2.33	5.2×10^{13}
	$C^{34}S$ 3-2	0.07	7.9×10^{11}
	$H^{13}CN$ 1-0	0.70	no data
	$H^{13}CN$ 2-1	not detected	
SMM6	CN 1-0	11.48	2.4×10^{15}
	HCN 1-0	11.85	3.4×10^{14}
	CS 3-2	9.37	1.1×10^{14}
	$C^{34}S$ 3-2	0.54	6.4×10^{12}
	$H^{13}CN$ 1-0	0.16	no data
	$H^{13}CN$ 2-1	0.02	no data
SMM9	CN 1-0	4.82	9.9×10^{14}
	HCN 1-0	12.55	3.1×10^{14}
	CS 3-2	13.75	1.7×10^{14}
	$C^{34}S$ 3-2	1.17	1.4×10^{13}
	$H^{13}CN$ 1-0	1.61	no data
	$H^{13}CN$ 2-1	0.04	no data
SMM10	CN 1-0	2.89	5.9×10^{14}
	HCN 1-0	4.40	1.3×10^{14}
	CS 3-2	4.47	5.1×10^{13}
	$C^{34}S$ 3-2	0.35	4.2×10^{12}
	$H^{13}CN$ 1-0	0.98	no data
	$H^{13}CN$ 2-1	not detected	
SMM12	CN 1-0	10.58	2.2×10^{15}
	HCN 1-0	13.98	4.0×10^{14}
	CS 3-2	10.30	1.2×10^{14}
	$C^{34}S$ 3-2	0.93	1.1×10^{13}
	$H^{13}CN$ 1-0	2.46	no data
	$H^{13}CN$ 2-1	not detected	

a Line frequency at the main peak position.
b Integrated flux above 3σ.

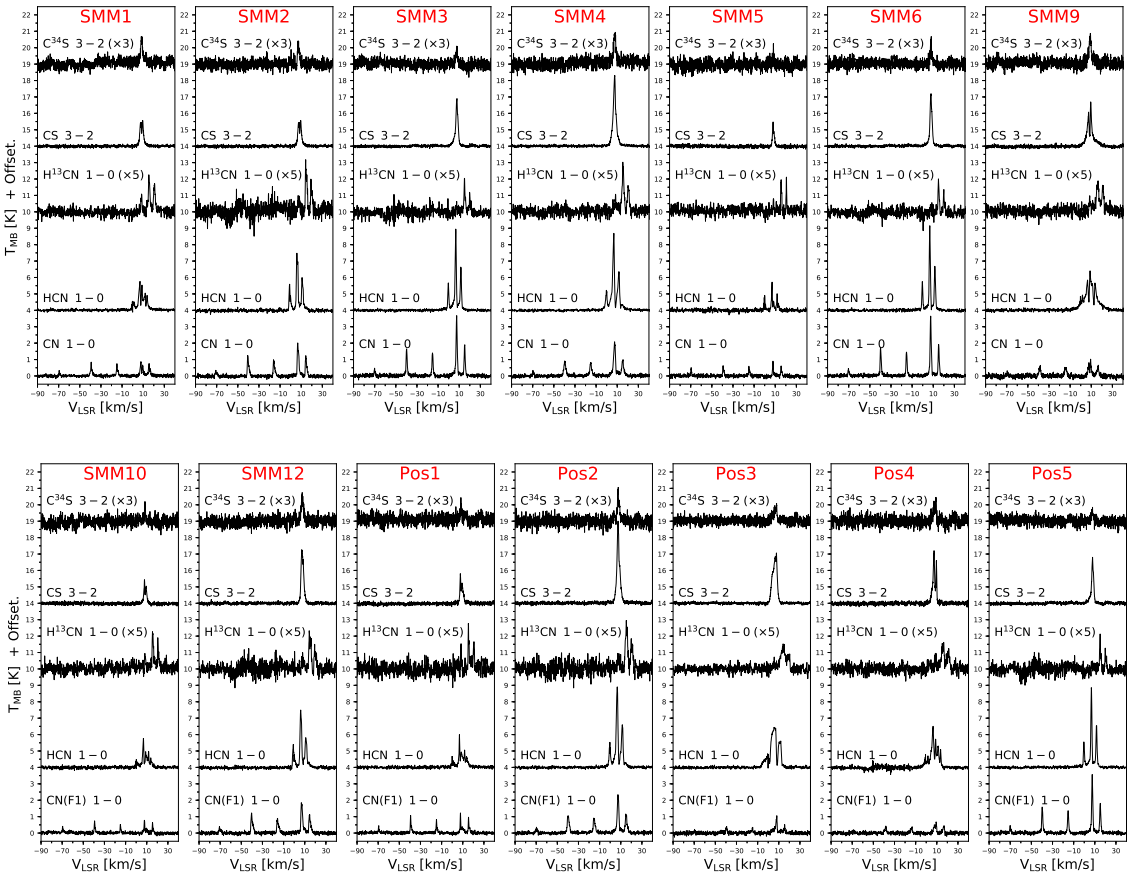

Fig. 7. Serpens Main sources spectra of $C^{34}S$ $J = 3 - 2$, CS $J = 3 - 2$, $H^{13}CN$ $J = 1 - 0$, HCN $J = 1 - 0$ and CN $J = 1 - 0$ lines.

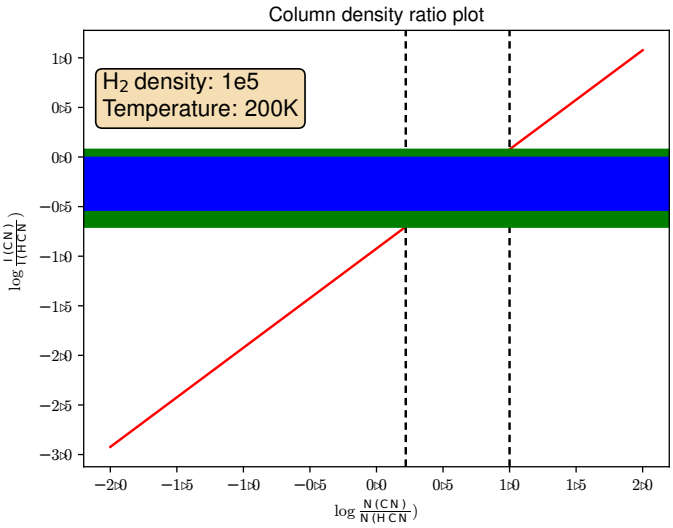

Fig. 8. RADEX model predictions for the CN/HCN column density ratio for hydrogen densities of $n_{H_2} = 10^5$ cm^{-3} and kinetic temperatures of $T_{kin} = 200$ K (red line). The observed line intensity ratio is plotted in blue (protostars positions) and green (all positions).

ciated, while CN cannot. This leads to higher abundance of CN molecules and increases CN/HCN column density ratio.

We used Nahoon code (Wakelam et al. 2012) that model the time evolution of 474 species involving gas-phase and gas-grain reactions with fixed temperature, density, UV, and cosmic ray fluxes. The evolution of CN, HCN and CS abundances was started at the time of a dense cloud formation. The UV radiation is described in the code by A_V parameter through the relation between visual extinction and the photodissociation rate coefficient:

$$k = \alpha e^{-\gamma A_V} \quad (5)$$

where α and γ are coefficients of the photodissociation process. In case of photodissociation HCN the coefficients equal 1.64×10^{-9} and 3.12 respectively (Heays et al. 2017).

The first model (Fig. 9) was established for a typical dense cloud with temperature of 10 K and hydrogen total density of $n_{HI+H_2} = 10^4$ cm^{-3}. The chemical composition of the studied molecules stabilises at the time of 10^7 yrs with HCN higher abundance in respect to CN molecule. We assumed the time of

Table 5. RADEX calculations of CN/HCN column density ratio

n_{H_2} [cm^{-3}]	T_{kin} [K]	$\log_{10}$(N[CN]/N[HCN])
10^3	30	0.03-0.88
10^3	75	0.06-0.84
10^3	200	0.00-0.78
10^4	30	0.16-0.94
10^4	75	0.08-0.86
10^4	200	0.04-0.82
10^5	30	0.20-0.98
10^5	75	0.18-0.86
10^5	200	0.22-1.00

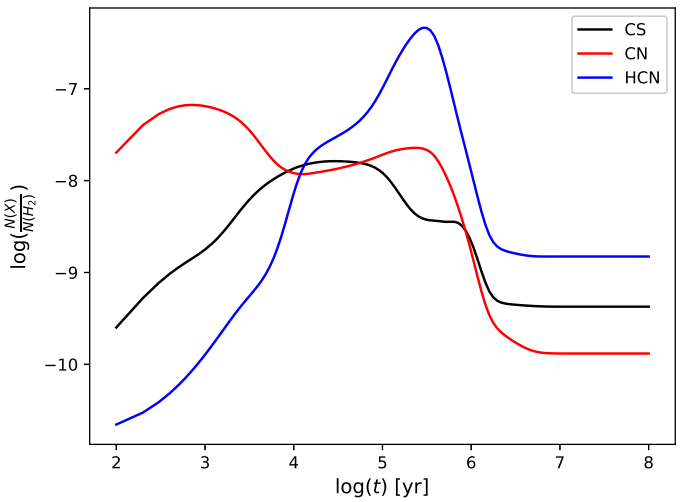

Fig. 9. Time evolution of CN (red line), HCN (blue line) and CS (black line) abundances obtained with Nohoon astrochemical code with initial parameters of $n_{\mathrm{HI+H_2}} = 10^4$ cm^{-3}, $T = 10$ K, $A_{\mathrm{V}} = 5^{\mathrm{m}}$. The other parameters remained defaulted: cosmic-ray ionization rate of 1.3×10^{17} s^{-1}, dust to gas mass ratio of 0.01, dust grain radius of 10^{-5} cm, grain density of 3 g cm^{-3}.

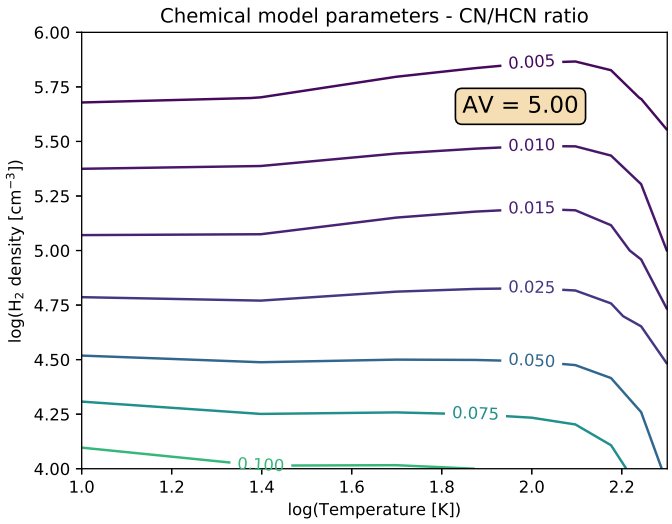

Fig. 10. Contour plot of Nahoon sets of models of CN/HCN abudances ratio with fixed visual extinction $A_{\mathrm{V}} = 5^{\mathrm{m}}$ at the time of 1.063×10^7 yrs after star formation began in the cloud. The other parameters remained defaulted: cosmic-ray ionization rate of 1.3×10^{17} s^{-1}, dust to gas mass ratio of 0.01, dust grain radius of 10^{-5} cm, grain density of 3 g cm^{-3}.

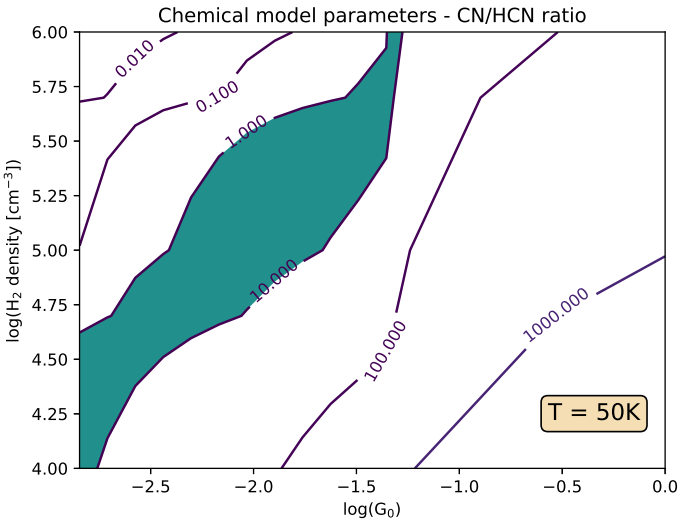

Fig. 11. Contour plot of Nahoon sets of models of CN/HCN abudances ratio with fixed temperature $T = 50$ K at the time of 1.063×10^7 yrs after star formation began in the cloud. The other parameters remained defaulted: cosmic-ray ionization rate of 1.3×10^{17} s^{-1}, dust to gas mass ratio of 0.01, dust grain radius of 10^{-5} cm, grain density of 3 g cm^{-3}. The observational column density ratio is marked with blue colour.

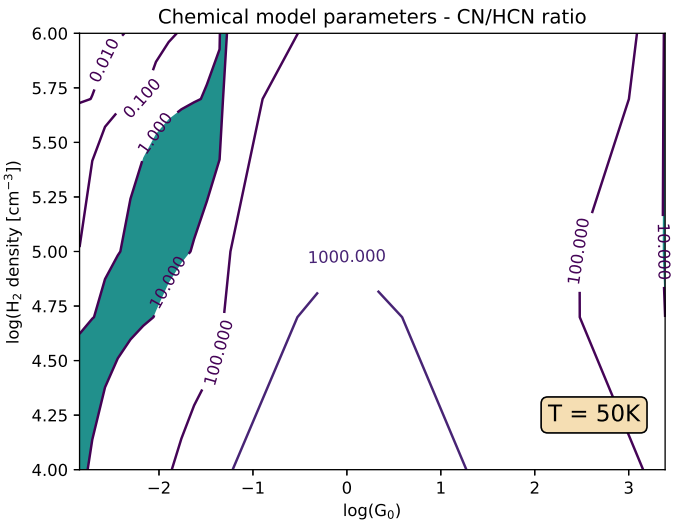

Fig. 12. Contour plot of Nahoon sets of models of CN/HCN abudances ratio with fixed temperature $T = 50$ K at the time of 1.063×10^7 yrs after star formation began in the cloud. The other parameters remained defaulted: cosmic-ray ionization rate of 1.3×10^{17} s^{-1}, dust to gas mass ratio of 0.01, dust grain radius of 10^{-5} cm, grain density of 3 g cm^{-3}. The observational column density ratio is marked with blue colour.

10^6 yrs as the time when the star formation starts in dense clouds. The modelled abundances of the all 474 species at the time of 10^6 yrs were used as an input data for the following set of models.

In the next models the closest neighbourhood of low-mass protostars was simulated. The initial abundances of all species available in Nahoon code were calculated based on the first model. We adopted the UV radiation and cosmic ray fluxes typical for dense clouds as an initial conditions. The visual extinction and the total cosmic-ray ionization rate were set as 5^{m} and 1.3×10^{17} s^{-1} respectively. The sets of models were run for the temperature range between 10 and 200 K and the total hydrogen densities from 10^4 cm^{-3} to 10^6 cm^{-3}. The resulting ratio of CN and HCN abundances is shown in Fig. 10. The results are consistent with starless cloud model (Fig. 9). Without any additional source of the UV radiation the HCN is more abundant molecule then CN about 2-3 orders of magnitude. Moreover, the CN/HCN abundances ratio is slightly dependent on gas temperature up to 150 K.

This results justify assumptions for the next set of models. The fixed gas temperature of 50 K was set. The models were run for the range of visual extinction between 1^{m} and 2.1^{m} what

corresponds to the UV radiation field of 0.044 to 0.001 G_0. The computed CN/HCN abundances ratio is presented in Fig. 11. The additional UV radiation of the strength of few thousandth of the average interstellar UV radiation field is enough to cover the observations in wide range of total hydrogen densities.

An additional source of the UV radiation was needed to reproduce the observational CN/HCN abundances what leads to conclusion that there is non-zero UV radiation field around low-mass protostars.

Acknowledgements. AM, AK and MG are supported by the Polish National Science Center grants 2013/11/N/ST9/00400 and 2016/21/D/ST9/01098. This research has made use of data from the Herschel Gould Belt survey (HGBS) project (http://gouldbelt-herschel.cea.fr). The HGBS is a Herschel Key Programme jointly carried out by SPIRE Specialist Astronomy Group 3 (SAG 3), scientists of several institutes in the PACS Consortium (CEA Saclay, INAF-IFSI Rome and INAF-Arcetri, KU Leuven, MPIA Heidelberg), and scientists of the Herschel Science Center (HSC).

References

Suresh, A., Dunham, M. M., Arce, H. G., et al. 2016, AJ, 152, 36

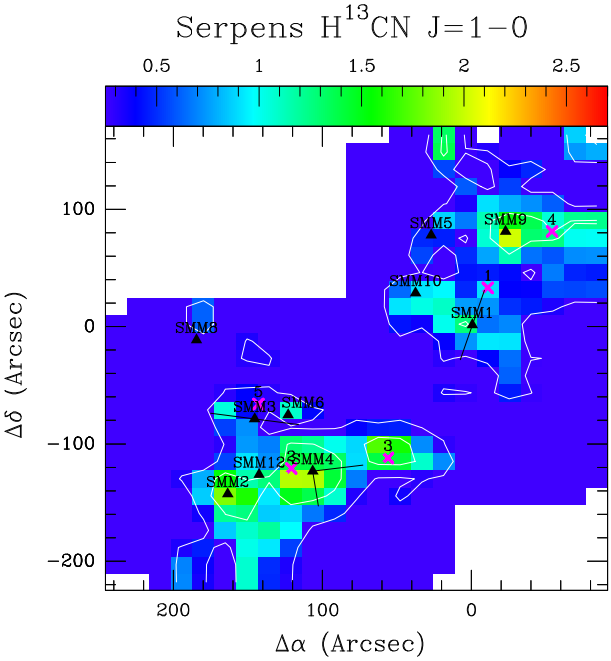

Fig. A.1. Similar to Fig. 3 but the emission of the $H^{13}CN$ $J = 1 - 0$ line.

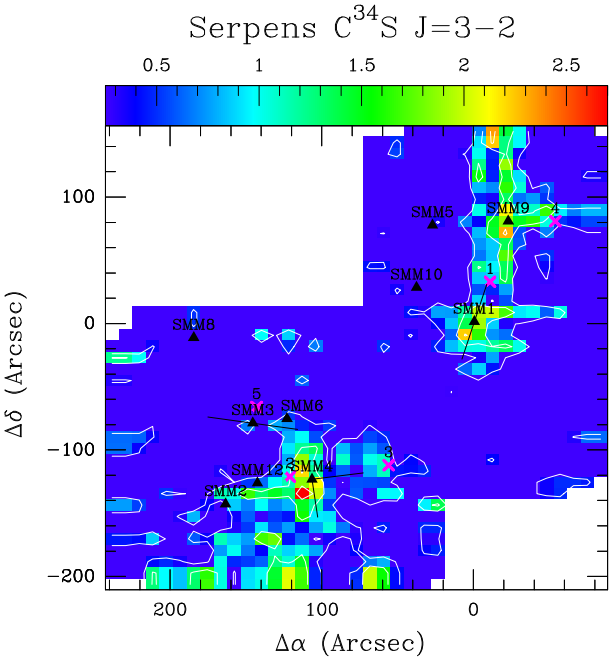

Fig. A.2. Similar to Fig. 3 but the emission of the $C^{34}S$ $J = 3 - 2$ line.

Appendix A: Molecular emission maps